TOPICAL REVIEW — Quantum information

Graphene-like physics in optical lattices*

Mei Feng(梅 锋)[a], Zhang Dan-Wei(张丹伟)[b], and Zhu Shi-Liang(朱诗亮)[a]†

[a] National Laboratory of Solid State Microstructures and School of Physics, Nanjing University, Nanjing 210093, China
[b] Laboratory of Quantum Engineering and Quantum Materials, School of Physics and Telecommunication Engineering, South China Normal University, Guangzhou 510006, China

(Received 28 September 2013; revised manuscript received 18 October 2013)

Graphene has attracted enormous attention over the past years in condensed matter physics. The most interesting feature of graphene is that its low-energy excitations are relativistic Dirac fermions. Such feature is the origin of many topological properties in graphene-like physics. On the other hand, ultracold quantum gas trapped in an optical lattice has become a unique setting for quantum simulation of condensed matter physics. Here, we mainly review our recent work on quantum simulation of graphene-like physics with ultracold atoms trapped in a honeycomb or square optical lattice, including the simulation of Dirac fermions and quantum Hall effect with and without Landau levels. We also present the related experimental advances.

Keywords: graphene, Dirac fermions, quantum Hall effect, optical lattice

PACS: 61.48.Gh, 73.43.–f, 37.10.Jk **DOI:** 10.1088/1674-1056/22/11/116106

1. Introduction

Graphene is a monolayer of carbon atoms packed into a dense honeycomb crystal structure. This material was presumed not to exist in the free state and has not been isolated experimentally until recently.[1] It is the first example of truly two-dimensional material and now has attracted tremendous interest in material science and condensed matter physics.[2,3] One of the most interesting aspects of graphene physics is that its low-energy excitations are massless Dirac fermions.[4,5] In the low-energy limit, the band structure of graphene can be approximated as two Dirac cones located at two inequivalent Brillouin zone corners. The energy dispersion relation in these cones is linear and the electron dynamics can be treated as relativistic. Therefore, graphene can provide a new platform for testing relativistic quantum electrodynamics.[6]

The presence of such Dirac feature in graphene is also expected to lead to a number of unusual electronic properties such as the unconventional quantum Hall effect.[7] In the presence of a magnetic field, the energy spectrum of graphene is rearranged into Landau levels (LLs). Due to the presence of valley and spin degrees of freedom, each LL is approximately four-fold degenerate. The underlying Dirac structure gives rise to an unconventional quantum Hall sequence $\sigma_{xy} = \pm 4e^2/h(n+1/2)$, where n is the LL index and the factor 4 denotes the double valley and spin degeneracy. The unusual Hall sequence is now well understood and found to arise from the fact that the zero-energy LL has half of the higher LLs' degeneracy.[8] Experimentally, such a ladder of Landau levels exhibits itself in the observation of unconventional quantum Hall plateaus.[9,10]

Graphene is also related to the birth of topological insulator, which now has become the forefront of condensed matter physics. In 1988, Haldane showed that electrons hopping on a graphene lattice can exhibit the integer quantum Hall effect without Landau levels.[11] In that model, a complex-valued next-nearest-neighbor (NNN) hopping was introduced to break the time-reversal symmetry. This two-band system has nontrivial topology and can be characterized by the topological Chern numbers. By tuning the NNN hopping strength, one can open an energy gap at the Dirac points and produce the quantum anomalous Hall effect. Haldane model is the first model that predicted topological insulator presenting the QHE without LLs, which opens the door for the final prediction and discovery of Z_2 topological insulator.[12]

On the other hand, ultracold atoms trapped in optical lattices nowadays are widely recognized as powerful experimental tools for mimicking a wide range of systems originally stemming from condensed matter physics.[13,14] These systems can provide a highly controllable environment and reach many extreme physical situations unachieved in solids. Many significant experimental advances have been made in this direction. Specifically, mimicking gauge fields and relativistic quantum phenomena has recently attracted much attention.[15,16] In particular, for ultracold atoms in optical lattices, the group of Esslinger in ETH has realized a tunable graphene-like honeycomb optical lattice and observed the related topological phase transition between massless

*Project supported by the National Natural Science Foundation of China (Grant No. 11125417), the State Key Program for Basic Research of China (Grant No. 2011CB922104), and the PCSIRT. DWZ was also supported by the SRFGS of SCNU.

†Corresponding author. E-mail: slzhunju@163.com

© 2013 Chinese Physical Society and IOP Publishing Ltd

and massive Dirac fermions,[17] which was revealed theoretically in Ref. [18]. Moreover, by using the optical dressing method,[15] several groups have successfully generated the artificial Abelian and non-Abelian gauge fields in ultracold atoms,[19–29] observed the Zitterbewegung effect,[30,31] and the spin Hall effect.[32–34] These theoretical and experimental advances pave the way to study some topological phases of matter related to relativistic Dirac fermions with well-controllable experimental parameters.

In this paper, we mainly review our recent theoretical work on quantum simulation of graphene-like physics with ultracold atoms and present the involved experimental demonstration. This review is organized as follows. In Section 2, we firstly describe our theoretical work on mimicking graphene and observing the related topological phase transitions between massless and massive Dirac fermions with ultracold femionic atoms in a honeycomb optical lattice, and then show the recent experimental demonstration. In Section 3, we review that the unconventional Hall effect in graphene can be simulated with ultracold atoms in a square optical lattice and the contribution of single Dirac cone to the Hall conductivity can be detected. In Section 4, we show that the quantum anomalous Hall effect (Haldane model) in graphene lattice can be realized and detected with ultracold atoms trapped in a honeycomb optical lattice and subjected to a laser-induced staggered magnetic field. In Section 5, we give a short summary on this review.

2. Dirac fermions in optical lattice

Ultracold atoms loaded into a hexagonal optical lattice was proposed to simulate Dirac fermions in 2007 by our group.[18] In that paper, we further found that, by controlling the lattice anisotropy, one can realize both massive and massless Dirac fermions and observe the topological phase transition between them. There are two (zero) Dirac points in the phase of massless (massive) Dirac particles, and each Dirac point is characterized by a topological winding number ± 1 and related to a quantized (topological) Berry phase $\pm\pi$. In this scene, the phase transition between massive and massless Dirac particles can be considered as a topological phase transition, which separates the phases characterized by different winding numbers.[35] The experimental possibility of this proposal has been analyzed in detail in Ref. [36]. Even in the presence of a harmonic confining potential, the Dirac points are also found to survive.[37] In the presence of atomic interactions, the many-body physics of Dirac fermions has been extensively studied in honeycomb lattice, including the BCS–BEC crossover,[38] the superfluidity at the Dirac point,[39] the topological phase transition[40–42] and even charge and bond ordered states with p-orbital band of lattices.[43] Experimentally, the simulation of Dirac fermions and observation of the topological phase transition between massless and massive Dirac particles through applying a controlled anisotropy on the structure, as predicted in Ref. [18], have been demonstrated in several systems, such as a tunable honeycomb optical lattice,[17] molecule lattice,[44] as well as microwave lattices.[45]

In this section, we focus on reviewing our theoretical work on quantum simulation of Dirac fermions.[18] We first show that Dirac fermions could be mimicked in a graphene-like honeycomb optical lattice and detected by measuring the Bragg spectroscopy and the atomic density profile. Then, we present the experimental results of ETH group on engineering and detecting Dirac points in a tunable honeycomb optical lattice.[17]

2.1. Simulation of Dirac fermions

Let us consider single-component fermionic atoms loaded in a hexagonal optical lattice. This lattice can be generated with three detuned standing wave lasers and has the potential

$$V(x,y)=\sum_{j=1,2,3}V_j^0\sin^2\left[k_{\rm L}(x\cos\theta_j+y\sin\theta_j)+\frac{\pi}{2}\right], \quad (1)$$

where $\theta_1=\pi/3$, $\theta_2=2\pi/3$, $\theta_3=0$, and $k_{\rm L}$ is the optical wave number. As shown in Figs. 1(a) and 1(b), it is easy to tune the hexagonal lattice into a standard isotropic form or an anisotropic form by varying the laser intensities along different directions. From Fig. 1(c), one can find that a hexagonal lattice consists of two sublattices denoted by A and B. For single-component fermionic atoms, the atomic collisions are negligible at low temperatures. The tight-binding Hamiltonian of the system is then given by

$$H=-\sum_{\langle i,j\rangle}t_{ij}(a_i^\dagger b_j+{\rm H.c.}), \quad (2)$$

where $\langle i,j\rangle$ represents the neighboring sites, a_i and b_j denote the fermionic mode operators for the sublattices A and B, respectively. The tunneling rates t_{ij} depend on the tunneling directions in an anisotropic hexagonal lattice, and we denote them as t_1, t_2, and t_3 corresponding to the three different directions as described in Fig. 1(c). For simplicity, we assume $t_1=t_2=t$ and $t_3=\beta t$ with β being the anisotropy parameter. The first Brillouin zone of this system has also a hexagonal shape in the momentum space (see Fig. 1(d)). Two of the six corners in Fig. 1(d) are inequivalent and usually denoted as K and K'. One can choose $\boldsymbol{K}=(2\pi/a)(1/\sqrt{3},1)$ and $\boldsymbol{K}'=-\boldsymbol{K}$, where $a=2\pi/(\sqrt{3}k_{\rm L})$ is the lattice spacing. The Hamiltonian (2) can be diagonalized and the energy spectrum of the system has the expression of

$$E_{\boldsymbol{k}}=\pm t\sqrt{2+\beta^2+2\cos(k_y a)+4\beta\cos(\sqrt{3}k_x a/2)\cos(k_y a/2)}. \quad (3)$$

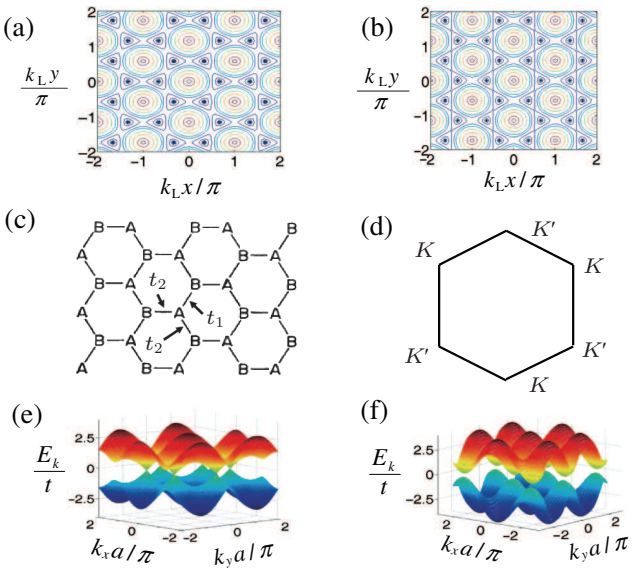


Fig. 1. (a) and (b) The optical potentials for producing a honeycomb optical lattice. The minima of the potentials are denoted by the solid dots. All V_j^0 are the same in (a), and $V_1^0 = V_2^0 = 0.91V_3^0$ in (b). (c) Decomposition of the hexagonal lattice as two triangular sublattices A and B with anisotropic tunneling. (d) The Brillouin zone of the hexagonal lattice. The dispersion relations are shown in (e) for $\beta = 1$ (gapless state) and (f) for $\beta = 2.5$ (gapped state).[18]

The energy spectra are plotted in Figs. 1(e) and 1(f). When $0 < \beta < 2$, the two branches touch each other and there appears a Dirac cone structure around the touching points. The two Dirac cones have the same form as that in graphene when $\beta = 1$ and squeeze in the x or y direction when β deviates from 1, but they still touch each other. Note that the merging and aligning of Dirac points were also discussed in a shaken honeycomb lattice recently.[46] When $\beta > 2$, a finite energy gap $\Delta_g = |t|(\beta - 2)$ appears between the two branches. Thus, across the point $\beta = 2$, the topology of the Fermi surface changes and there appears a topological phase transition without any usual symmetry breaking.[18,47] With this topological phase transition, the system changes its behavior from a semimetal to an insulator at the half filling case. Around the half filling, the Fermi surface is close to the touching points, and one can expand the momentum $\boldsymbol{k}$ around one of the touching points $\boldsymbol{K} \equiv (k_x^0, k_y^0)$ as $(k_x, k_y) = (k_x^0 + q_x, k_y^0 + q_y)$. Up to the second order of q_x and q_y, the dispersion relation (3) becomes

$$E_{\mathbf{q}} = \pm\sqrt{\Delta_g^2 + v_x^2 q_x^2 + v_y^2 q_y^2}, \tag{4}$$

where $\Delta_g = 0$, $v_x = \sqrt{3}\beta ta/2$, and $v_y = ta\sqrt{1-\beta^2/4}$ for $0 < \beta < 2$; $\Delta_g = |t|(\beta - 2)$, $v_x = ta\sqrt{3\beta/2}$, and $v_y = ta\sqrt{\beta/2 - 1}$ for $\beta > 2$. Compared with the standard energy–momentum relation for the relativistic Dirac particles, here Δ_g and $v_{x,y}$ take the meanings of rest energy and the velocity of light, respectively. The wave function for the quasiparticles around the half filling then satisfies the Dirac equation $i\hbar\partial_t \Psi = \mathscr{H}_D \Psi$, where the relativistic Hamiltonian H_D is given by

$$H_D = v_x \sigma_x p_x + v_y \sigma_y p_y + \Delta_g \sigma_z, \tag{5}$$

with $\sigma_{x,y,z}$ denoting the three Pauli matrices. By tuning the anisotropy parameter β, the quasiparticles in this system can change themselves from massless to massive Dirac fermions.

It is interesting to note that, apart from the hexagonal optical lattice, optical lattices with other structures of symmetries can also be used to simulate the two-dimensional relativistic Dirac fermions. For example, it is also proposed to simulate Dirac fermions in a so-called $\mathscr{T}_3$ optical lattice,[48,49] in a line-centered-square optical lattice,[50] and even in a simple square optical lattice combing with a synthetic gauge potential.[51–58] One may also simulate three-dimensional analog of Dirac quasiparticles with cold atoms properly loaded in some cubic optical lattices.[59–61] Without optical lattices, relativistic quasiparticles and related novel effects in bulk atomic gases within the light-induced gauge fields[15] have also attracted much attention.[30,31,62–70]

2.2. Detection of Dirac fermions

In the following, we will show how to conform the relativistic quasiparticles and the topological phase transition with the density profile measurement[71,72] and the Bragg spectroscopy.[73]

2.2.1. Density profile measurement

The density profile of the trapped atoms can be measured through the time-of-flight imaging with the light absorption. One can reconstruct the initial real-space density profile of the trapped gas from the final measured absorption images. Under the local density approximation, the local chemical potential varies with the radial coordinate by $\mu = \mu_0 - V(\boldsymbol{r})$, where μ_0 is the chemical potential at the trap center and $V(\boldsymbol{r}) = m\omega^2 \boldsymbol{r}^2/2$ is the global harmonic trapping potential. At temperature T, the atomic density is given by

$$n(\mu) = \frac{1}{S_0}\int f(k_x, k_y, \mu)\,\mathrm{d}k_x\,\mathrm{d}k_y, \tag{6}$$

where $S_0 = 8\pi^2/\sqrt{3}a^2$ is the area of the first Brillouin zone of the hexagonal lattice, and $f(k_x, k_y, \mu) = 1/\{\exp[(E_{\boldsymbol{k}} - \mu)/T] + 1\}$ ($E_{\boldsymbol{k}}$ in Eq. (3)) is the Fermi–Dirac distribution. At low temperature ($T \sim 0$), this density profile $n(\mu)$ is shown in Figs. 2(a) and 2(b) for the parameters with massless and massive Dirac quasiparticles, respectively. Clearly, a plateau at the atom density $n = 1$ in the density profile appears for the gapped phase with massive Dirac fermions, but there is no such a plateau for the case with massless Dirac fermions. Thus, the plateau is associated with massive quasiparticles, and its emergence provides an unambiguous signal for the phase transition between the two cases. Furthermore, the linear dispersion relation for the massless Dirac fermions can be confirmed by the derivative $\mathrm{d}n/\mathrm{d}\mu$ since one has $\partial n/\partial\mu = (4\pi/v^2 S_0)\,|\delta\mu|$ around the Dirac cone. As shown in Figs. 2(c) and 2(d), for the

case with massless Dirac fermions, $\partial n/\partial\mu$ is indeed linearly proportional to $\delta\mu$ at the vicinity of the half filling. Therefore, experimentally, from the measured density profile $n(\mu)$, one can determine its slope to confirm the massless Dirac fermions.

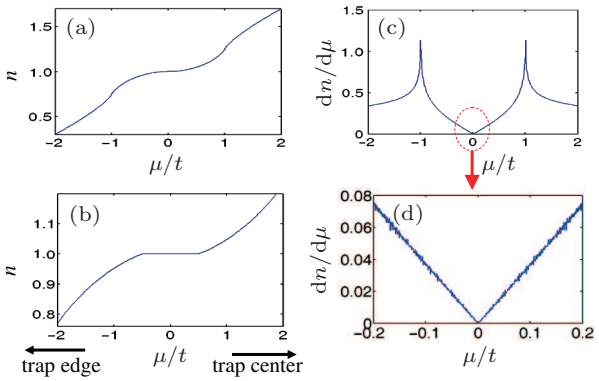


Fig. 2. The number density of atoms n per unit cell as a function of the chemical potential μ for (a) $\beta = 1$ and (b) $\beta = 2.5$. (c) The derivative $\mathrm{d}n/\mathrm{d}\mu$ as a function of the chemical potential μ for $\beta = 1$. (d) An enlarged part of $\mathrm{d}n/\mathrm{d}\mu$ at the vicinity of $\mu = 0$. The linearity of the curve shows the linear dispersion relation for the quasiparticles.[18]

2.2.2. Bragg spectroscopy

The Bragg spectroscopy can provide an alternative and complementary method to confirm the linear dispersion relation for the massless Dirac fermions and the energy gap for the massive ones. In Bragg spectroscopy, one shines two laser beams on the atomic gas as shown in Fig. 3(a). By fixing the angle between the two beams (thus fixing the relative momentum transfer $\boldsymbol{q} = \boldsymbol{k}_2 - \boldsymbol{k}_1$, where $\boldsymbol{k}_i$ denotes the wave vector of each laser beam), one can measure the atomic transition rate by scanning the laser frequency difference $\omega = \omega_2 - \omega_1$. From Fermi's golden rule, this transition rate basically measures the following dynamical structure factor:

$$S(\boldsymbol{q},\omega) = \sum_{\boldsymbol{k}_1,\boldsymbol{k}_2} |\langle f_{\boldsymbol{k}_2}|H_{\mathrm{B}}|i_{\boldsymbol{k}_1}\rangle|^2 \delta[\hbar\omega - E_{f\boldsymbol{k}_2} + E_{\mathrm{i}\boldsymbol{k}_1}], \quad (7)$$

where $H_{\mathrm{B}} = \sum_{\boldsymbol{k}_1,\boldsymbol{k}_2} \Omega\, \mathrm{e}^{\mathrm{i}\boldsymbol{q}\cdot r}|i_{\boldsymbol{k}_1}\rangle\langle f_{\boldsymbol{k}_2}| + \mathrm{h.c.}$ is the light–atom interaction Hamiltonian, and $|i_{\boldsymbol{k}_1}\rangle$ and $|f_{\boldsymbol{k}_2}\rangle$ denote the initial and the final atomic states with the energies $E_{\mathrm{i}\boldsymbol{k}_1}$ and $E_{\mathrm{f}\boldsymbol{k}_2}$ and the momenta $\boldsymbol{k}_1$ and $\boldsymbol{k}_2$, respectively. At the half filling, the excitations are dominantly around the touching point, and we can use the approximate dispersion relation in Eq. (4). For the isotropic case ($\beta = 1$) with massless Dirac Fermions, $S(q,\omega)$ has the expression of

$$S(q,\omega) = \frac{\pi\Omega^2}{8v_{\mathrm{F}}}\frac{2q_{\mathrm{r}}^2 - q^2}{\sqrt{q_{\mathrm{r}}^2 - q^2}}\Theta(\omega - \omega_{\mathrm{r}}), \quad (8)$$

where Θ is the unit step function, $\omega_{\mathrm{r}} = qv_{\mathrm{F}}/\hbar$ ($q \equiv |\boldsymbol{q}|$), and $q_{\mathrm{r}} = \hbar\omega/v_{\mathrm{F}}$. This dynamical structure factor is shown in Fig. 3(b). Note that in this case, the lower cutoff frequency ω_{r} is linearly proportional to the momentum difference q, and ω_{r} vanishes when q tends to zero. For the anisotropic case with $\beta > 2$, the spectrum in Eq. (4) becomes quadratic with $E \approx \pm(\Delta + \hbar^2 q_x^2/2m_x + \hbar^2 q_y^2/2m_y)$ for small momentum transfer $\boldsymbol{q}$, where the effective mass $m_{x,y} = \hbar^2\Delta/v_{x,y}^2$. The dynamical structure factor in this non-relativistic limit becomes

$$S(q,\omega) = \frac{\pi\Omega^2\Delta}{2v_x v_y}\Theta(\omega - \omega_{\mathrm{c}}^{x,y}), \quad (9)$$

where $\omega_{\mathrm{c}}^{x,y} = 2\Delta + \hbar^2 q_{x,y}^2/4m_{x,y}$. Its form is shown in Fig. 3(b). The lower cutoff frequency $\omega_c^{x,y}$ in this case does not vanish as the momentum transfer goes to zero. This distinctive difference between the dynamical structure factors in Eqs. (8) and (9) can be used to distinguish the cases with massive or massless Dirac fermions.

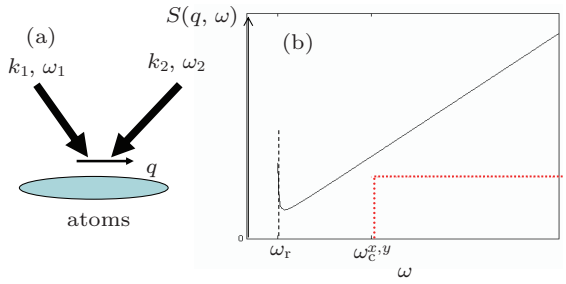


Fig. 3. Schematic of the Bragg scattering. (a) Atoms are illuminated by two laser beams with wave vectors $\boldsymbol{k}_1$, $\boldsymbol{k}_2$, and frequencies ω_1, ω_2, respectively. (b) The dynamic structure factors $S(\boldsymbol{q},\omega)$ for the massless Dirac fermions (solid line) and for the massive ones in the nonrelativistic limit (dotted line).[18]

2.3. Experimental demonstration

In this section, we will review the recent experiment by the ETH group on manipulating Dirac points with fermionic ^{40}K atoms loaded in a tunable honeycomb lattice.[17] By utilizing momentum-resolved interband transition, they further detect the Dirac fermions and identify the topological phase transition from massless to massive Dirac fermions.

2.3.1. Tunable optical lattice

We consider an ultracold Fermi gas of ^{40}K atoms loaded in a two-dimensional tunable optical lattice. As depicted in Fig. 4(a), this lattice is formed by three laser beams and has the potential of

$$\begin{aligned} V(x,y) = & -V_{\bar{X}}\cos^2(kx + \theta/2) - V_X\cos^2(kx) - V_Y\cos^2(ky) \\ & - 2\alpha\sqrt{V_X V_y}\cos(kx)\cos(ky)\cos(\varphi), \end{aligned} \quad (10)$$

where $V_{\bar{X}}, V_X$, and V_Y denote the single-beam lattice depths, α is the visibility of the interference pattern, and $k = 2\pi/\lambda$. One can adjust the two phases continuously and here choose $\theta = \pi$ and $\varphi = 0$. As shown in Fig. 4(b), various lattice structures can be realized by varying the relative intensities of the beams. For the honeycomb lattice, as plotted in Fig. 4(c), it consists of two sublattices and their energy offset can be controlled by the frequency detuning δ. As shown in Figs. 1(c) and 1(d), the

primitive lattice vectors are perpendicular, leading to a square Brillouin zone with two Dirac points inside. The presence of Dirac points in the band structure is identified by observing a minimum band gap inside the Brillouin zone using interband transitions.

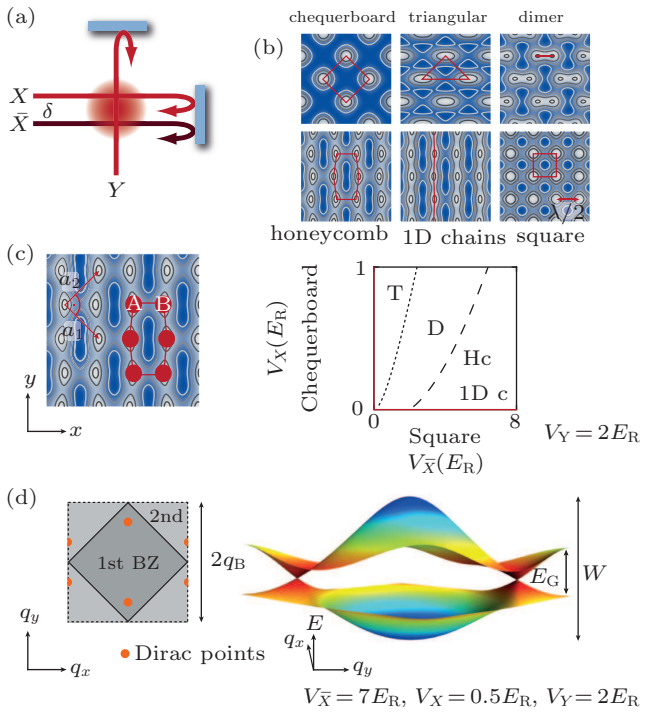


Fig. 4. (a) Three laser beams of wavelength $\lambda = 1064$ nm create the two-dimensional lattice potential of Eq. (10). (b) Top: different lattice potentials. Bottom: the accessible lattice geometries as a function of the lattice depths $V_{\bar{X}}$ and V_X. (c) The honeycomb lattice has a two-site unit cell. (d) Left: sketch of the first and second Brillouin zones, indicating the positions of the Dirac points. Right: three-dimensional view of the energy spectra. W is denoted as the full bandwidth, E_G as the minimum energy gap at the edges of the Brillouin zone, and $q_B = 2\pi/\lambda$ as the Bloch wavevector.[17]

2.3.2. Detection of Dirac points

The starting point of the experiment is a non-interacting, ultracold gas of $N \approx 50000$ fermionic ^{40}K atoms in the state $|F, m_F\rangle = |9/2, -9/2\rangle$, where F denotes the hyperfine manifold and m_F the Zeeman state. The cloud is prepared in the lowest-energy band of a honeycomb lattice. On application of a weak magnetic field gradient, the atomic cloud is subjected to a constant force F in the x direction, with an effect equivalent to that produced by an electric field in solid-state systems. The atoms are hence accelerated so that their quasi-momentum q_x increases linearly up to the edge of the Brillouin zone, where a Bragg reflection occurs. The cloud eventually returns to the center of the band, performing one full Bloch oscillation. Then, the quasi-momentum distribution of the atoms in different bands is measured.[74] In Fig. 5(a), for a trajectory far from the Dirac points (trajectory 1), the atoms remain in the lowest-energy band. In contrast, when passing through a Dirac point (trajectory 2), the atoms are transferred from the first band to the second because of the vanishing energy splitting at the linear band crossing. When measuring the quasi-momentum distribution, these atoms are missing in the first Brillouin zone and appear in the second band. The points of maximum transfer are identified with the Dirac points.

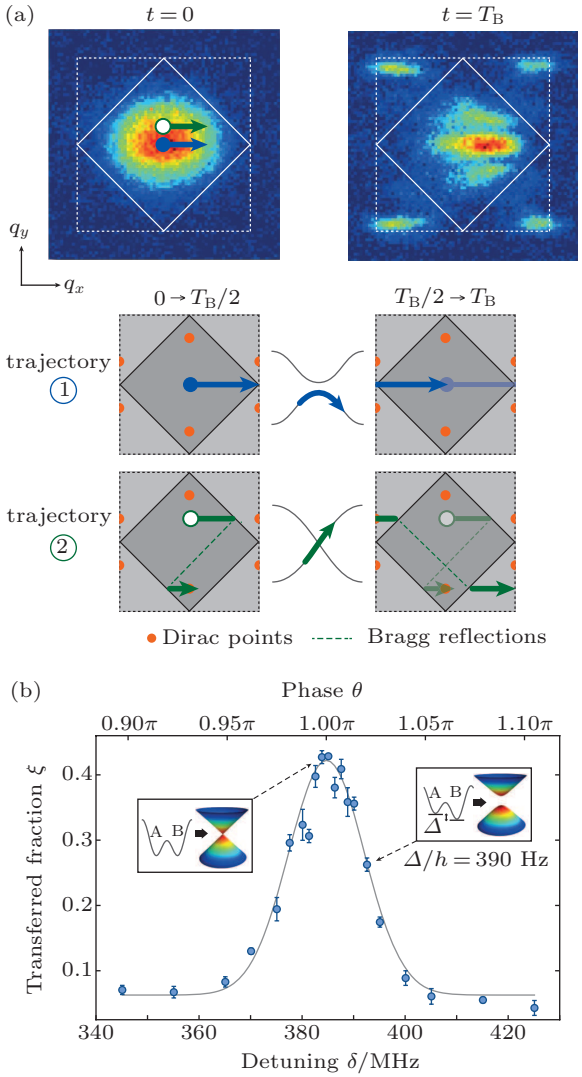


Fig. 5. (a) Quasi-momentum distribution of the atoms before and after one Bloch oscillation. (b) Dependence of the total fraction of atoms transferred to the second band on the detuning δ and phase θ which control the sublattice energy offset.[17]

To investigate how breaking the inversion symmetry of the lattice affects the Dirac points, the phase θ is tuned for changing the frequency detuning δ, then the sublattice offset Δ is varied. In Fig. 5(b), the total fraction of atoms transferred to the second band is measured and the results show a sharp maximum in the transferred fraction. This situation is referred to as the point of inversion symmetry and the bandgap at this point vanish. The population in the second band decreases symmetrically on both sides of the peak as the gap increases, indicating the transition from massless to massive Dirac fermions.

2.3.3. Detection of topological phase transition

In the experiment, the topological transition line is mapped out by recording the fraction of atoms transferred to the second band, as a function of the lattice depths $V_{\bar{X}}$ and V_X, while keeping V_Y fixed. The results are shown in Fig. 6(a). The onset of population transfer to the second band signals the appearance of Dirac points in the band structure of the lattice. For a given value of V_X, the transferred fraction decreases again for large values of $V_{\bar{X}}$, as the Dirac points lie beyond the momentum width of the cloud. To extend the range of the measurements and probe the Dirac points even in this region, a force in the y direction is applied. Along the q_y trajectories, the center of the cloud successively passes the two Dirac points during the Bloch cycle. As shown in Fig. 6(b), we again identify the topological transition by the onset of population transfer to the second band. At this transition, the transfer is expected to be lower by a factor of two along the central q_y trajectory, as compared to the central q_x trajectory. This is caused by the dispersion relation at the corners of the Brillouin zone being quadratic in the q_y direction and linear in q_x. One can find that, for both trajectories in Figs. 6(a) and 6(b), the onset of population transfer to the second band signals the topological transition, where the Dirac points appear.

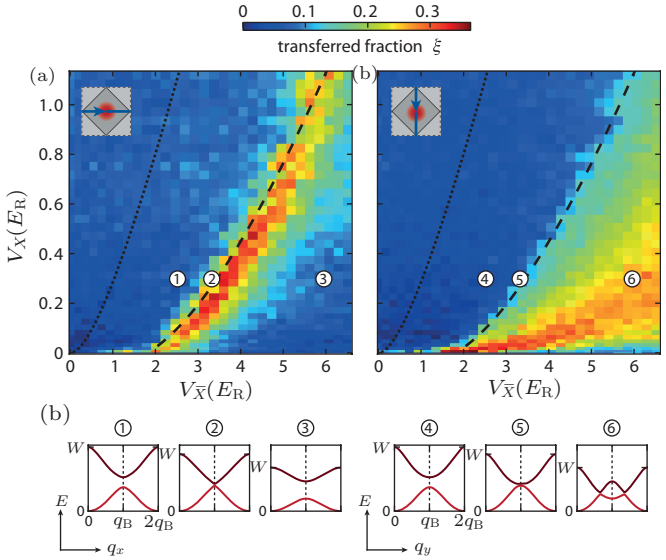


Fig. 6. Fraction of atoms transferred to the second band as a function of lattice depths $V_{\bar{X}}$ and V_X with $V_Y/E_R = 1.8(1)$, with trajectories in quasimomentum space in the q_x (a) and q_y (b) directions. Each data point is a single measurement, and as a result there are at least 1200 points per diagram. The dashed line is the theoretical prediction for the transition line without any fitting parameters. The bottom diagrams show cuts of the band structure along the (a) q_x axis and (b) q_y axis for the values of $V_{\bar{X}}$ and V_X.[17]

3. Unconventional quantum Hall effect in optical lattice

When the external magnetic field is applied, the Dirac fermions in graphene will lead to an unconventional Hall sequence.[8] In this section, we will review, with the help of laser-induced gauge field,[75] the unconventional quantum Hall effect in graphene can be simulated using ultracold atoms trapped in square optical lattice. It is also found that, by tuning the laser intensity to change the gauge fluxes, the energies of the four Dirac points in the first Brillouin zone are shifted from each other and the contribution of the single Dirac cone to the total atomic Hall conductivity can be detected. Notably, the laser-induced magnetic fields in two-dimensional square optical lattices and the Harper model have recently been demonstrated,[25–29] which paves the way to realize the quantum Hall state in optical lattices.

3.1. Square lattice model

We consider a two-component ultracold fermion gas trapped in a two-dimensional square optical lattice subjected to a gauge potential $\boldsymbol{A} = (A_x, A_y) = (\alpha\sigma_y, \beta\sigma_x + 2\pi\Phi m)$, where $\sigma_{x(y)}$ is the Pauli operator of the two atomic components, Φ is the uniform Abelian magnetic flux per unit cell and we set $c = \hbar = e = a = 1$. This gauge potential may be generated through laser-assisted hopping and the gauge fluxes (α, β) can be tuned via changing the laser field intensity.[56,76] The tight-binding Hamiltonian of the system is written as

$$H = -t\sum_{m,n}\left(c^{\dagger}_{m+1,n}e^{iA_x}c_{m,n} + c^{\dagger}_{m,n+1}e^{iA_y}c_{m,n}\right) + \text{H.c}, \quad (11)$$

where t is the nearest-neighbor hopping strength, and $c_{m,n}$ is a 2-component field operator. We firstly study the system in the non-Abelian gauge potential without external magnetic field ($\Phi = 0$). After diagonalizing the above Hamiltonian, the energy spectra has the form of

$$E_k = h_0(k) \pm \sqrt{h_x^2(k) + h_y^2(k)}, \quad (12)$$

where $h_0(k) = -2t(\cos(\alpha)\cos(k_x) + \cos(\beta)\cos(k_y))$, $h_x(k) = -2t\sin(\beta)\sin(k_y)$, and $h_y(k) = -2t\sin(\alpha)\sin(k_x)$. If the gauge fluxes $\alpha = \beta = \pi/2$, as shown in Fig. 7(a), the energy spectra has the same feature as graphene. There are four Dirac points in the first Brillouin zone, $\boldsymbol{k}_1 = (0,0)$, $\boldsymbol{k}_2 = (0,\pi)$, $\boldsymbol{k}_3 = (\pi,0)$, and $\boldsymbol{k}_4 = (\pi,\pi)$. In Fig. 8(a), under an external magnetic field (the induced flux $\Phi = 1/121$), we calculate the Hall plateaus against the Fermi energy and find that the Hall sequence does have the same unconventional form $\sigma_{xy} = 4(n+1/2)/h$ as in graphene. Therefore, the UQHE in graphene can be simulated with cold atoms trapped in optical lattice and subjected to laser-induced gauge field.

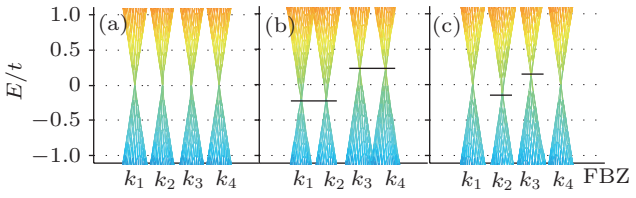


Fig. 7. The dispersion relations in the vicinity of the four Dirac cones in the FBZ with different parameters: α and β. (a) $\alpha = \beta = \pi/2$; (b) $\alpha = \pi/2 + 0.1$, $\beta = \pi/2$; (c) $\alpha = \pi/2 + 0.05$, $\beta = \pi/2 - 0.05$.[75]

Interestingly, apart from the conventional linear dispersion relation in the Dirac cone, the energies of the four Dirac points are

$$\delta E_{14} = \pm 2t(\cos\alpha + \cos\beta),$$
$$\delta E_{23} = \pm 2t(\cos\alpha - \cos\beta). \quad (13)$$

If the gauge fluxes deviate from $\alpha = \beta = \pi/2$, one can find that the positions of the four Dirac points will be shifted with each other but the characteristics of linear dispersion are still kept.[75] Based on this feature, we can manifest the contribution of single Dirac cone to the Hall conductivity as half-odd number sequences $n + 1/2$. The results in Figs. 7(b) and 7(c) show four and two Dirac points can be shifted with each other. The corresponding new Hall conductivities are calculated in Figs. 8(b) and 8(c). Each new Hall plateau corresponds to one of the new energy gaps induced by the energy shifts. When the Fermi energy lies in one of the new gaps, each shifted Dirac cone contributes to the Hall conductivity with a half-odd topological number. It is found that the sum of the four half-odd topological numbers corresponding to each gap is equal to the numerically calculated Chern number of the gap. Compared with the existing method, our setup proves a clearer and simpler fashion to achieve the signature of half-odd number sequences contributed from single Dirac cone.[77]

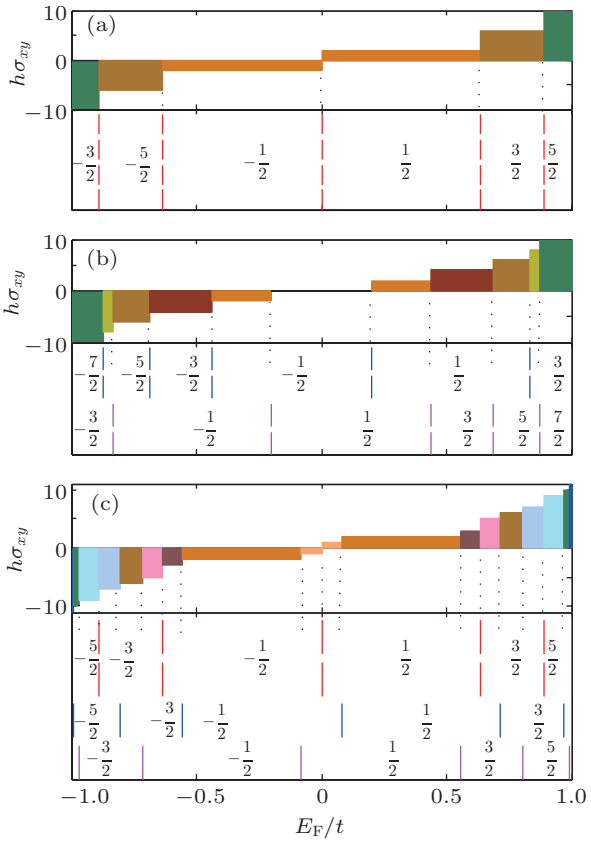


Fig. 8. The Hall plateaus against the Fermi energy for $\Phi = 1/121$ in the conditions of Fig. 1 (same indexing). For comparison, in the lower part of each figure, we also plot the relativistic LLs and the half-odd Chern numbers corresponding to each gap in the four Dirac cones.[75]

3.2. Detection of Hall conductivity

In cold atoms, the Hall conductivity is detected through density profile measurement discussed in Section 2.2.1. According to the Streda formula $\sigma_{xy} = \frac{1}{h}\frac{\partial n}{\partial \Phi}|_{E_F^l,T}$, to measure the Hall conductivity, we need to choose two magnetic flux values, and identify the plateaus in both density profiles that correspond to the same gap.[78–80] In Fig. 9, the atomic density profiles are plotted for the cases in Fig. 8, with $\Phi_1 = 1/121$, $\Phi_2 = 2/121$, and $\Delta\Phi = \Phi_2 - \Phi_1 = 1/121$. Through comparing the two density profiles, the atomic Hall conductivity can be derived as $h\sigma_{xy} = (n_2 - n_1)/\Delta\Phi$. We take Fig. 9(b) as an example to demonstrate the procedure to obtain the Hall plateaus. If the local Fermi energy lies in the energy gap with the Chern number 2, as shown in Fig. 8(b), one can find that the two densities of the gap are $n_2/\Delta\Phi = 125$ and $n_1/\Delta\Phi = 123$. Then, the corresponding atomic Hall conductivity is $\sigma_{xy} = (n_2 - n_1)/(h\Delta\Phi) = 2/h$, which yields the Chern number 2 and agrees with the result shown in Fig. 8(b).

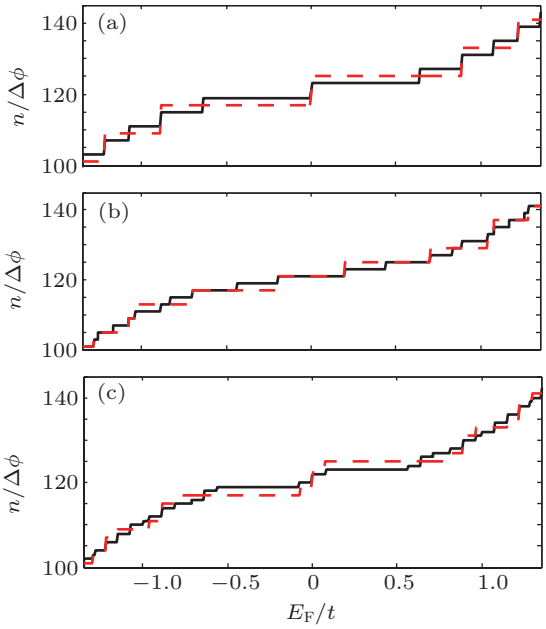


Fig. 9. The atomic density profiles $n(E_F^l)/\Delta\Phi$ against the local Fermi energy in the condition of Fig. 7. The solid (dash) line corresponds to $\Phi = 1/121$ (2/121).[75]

4. Quantum anomalous Hall effect in optical lattice

Haldane model is the first model that can provide an integer Hall effect without landau levels.[11] This model has been simulated with ultracold atoms trapped in a graphene-like s-band and p-band honeycomb optical lattices.[78,81,82] The staggered magnetic field in the Haldane model is generated through optical dressing and rotating lattice site, respectively. Besides, it was proposed to implement the Haldane model in a square optical superlattice.[57] Recently, it has been generalized to use laser-assisted hopping in a state-dependent optical lattice.[83,84] In this section, we mainly review our work

on mimicking Haldane model with s-band optical lattice.[78] Finally, we describe the detection method for measuring the Chern number in this simulation system.

4.1. Simulation of Haldane model

In Haldane's work, a tight-binding model on a honeycomb lattice including a complex second nearest-neighbor hopping integral is constructed. The honeycomb lattice consists of two triangular sublattices A and B with different on site energies M and $-M$, as shown in Fig. 10(a). A periodic vector potential $\boldsymbol{A}$ is applied to the lattice, given that the total magnetic flux through each unit cell vanishes, and the first neighbor hopping integral t is unaffected. The second neighbor hopping integral t' acquires a Peierls phase factor $\exp(\mathrm{i}\,\mathrm{e}\int \boldsymbol{A}\cdot \mathrm{d}\boldsymbol{r}/\hbar)$, where the integration is along the hopping path. The Hamiltonian of the model is written as

$$\begin{aligned} H &= \sum_{\langle i,j\rangle} t(a_i^{\dagger}b_j + \mathrm{H.c.}) + \sum_j M(a_j^{\dagger}a_j - b_j^{\dagger}b_j) \\ &+ \sum_{\langle\langle l,j\rangle\rangle} t' e^{i\varphi_{jl}}(a_l^{\dagger}a_j + b_l^{\dagger}b_j), \end{aligned} \tag{14}$$

where a_i and b_i are the annihilation operators on site R_i in sublattices A and B, respectively. φ_{jl} is the accumulated Peierls phase from site j to its second neighbor l, which is assumed to take the form $\varphi_{jl} = \pm\varphi$. The hopping directions for $\varphi_{jl} = +\varphi$ are shown in Fig. 10(a).

We consider single component fermionic atoms trapped in a 2D honeycomb lattice which can be realized by three detuned laser beams. A detuned standing-wave laser beam will create a potential in the form $V_0\sin^2(\boldsymbol{k}_0^{\mathrm{L}}\boldsymbol{r})$, where V_0 is the potential amplitude, and $\boldsymbol{k}_0^{\mathrm{L}}$ is the wave vector of the laser. In order to generate the honeycomb lattice with different on-site energies in sublattices A and B, the three laser beams with the same wave length but different polarizations are applied along three different directions: $\boldsymbol{e}_y$ and $\frac{\sqrt{3}}{2}\boldsymbol{e}_x \pm \frac{1}{2}\boldsymbol{e}_y$, respectively. The potential is thus given by $V = V_0[\sin^2(\alpha_+ + \pi/2) + \sin^2(k_0^{\mathrm{L}}y + \pi/3) + \sin^2(\alpha_- - \chi/2)]$, where $\alpha_\pm = \frac{\sqrt{3}}{2}k_0^{\mathrm{L}}x \pm \frac{1}{2}k_0^{\mathrm{L}}y$. The potential contours are plotted in Figs. 10(b) and 10(c). Under these conditions, atoms are trapped at the minima of the potential, forming a honeycomb lattice. An amazing feature here is that the different site energies of sublattices A and B are controllable by the phase of laser beam χ.

Now we elaborate how to simulate the staggered magnetic field in the Haldane model. Since the net flux per unit cell vanishes, the vector potential applied to the lattice must be periodic. Such magnetic fields can be created by the Berry phase induced from two opposite-traveling standing-wave laser beams.[32] For the two laser beams with Rabbi frequencies $\Omega_1 = \Omega_0\sin(k_2^{\mathrm{L}}y + \frac{\pi}{4})\,\mathrm{e}^{\mathrm{i}k_1^{\mathrm{L}}x}$ and $\Omega_2 = \Omega_0\cos(k_2^{\mathrm{L}}y + \frac{\pi}{4})\,\mathrm{e}^{-\mathrm{i}k_1^{\mathrm{L}}x}$, where $k_1^{\mathrm{L}} = k^{\mathrm{L}}\cos\theta$ and $k_2^{\mathrm{L}} = k^{\mathrm{L}}\sin\theta$ with k^{L} being the wave vector of the laser and θ the angle between the wave vector and the $\boldsymbol{e}_x$ axis, the total vector potential and magnetic field can be written as

$$\begin{aligned} \boldsymbol{A} &= \hbar k_1^{\mathrm{L}}[\sin(2k_2^{\mathrm{L}}y) + \cos(\sqrt{3}k_2^{\mathrm{L}}x)\sin(k_2^{\mathrm{L}}y)]\boldsymbol{e}_x \\ &\quad - \sqrt{(3)}\hbar k_1^{\mathrm{L}}\sin(\sqrt{3}k_2^{\mathrm{L}}x)\cos(k_2^{\mathrm{L}}y)\boldsymbol{e}_y, \\ \boldsymbol{B} &= -2\hbar k_1^{\mathrm{L}}k_2^{\mathrm{L}}[\cos(2k_2^{\mathrm{L}}y) \\ &\quad + 2\cos(\sqrt{3}k_2^{\mathrm{L}}x)\cos(k_2^{\mathrm{L}}y)]\boldsymbol{e}_z. \end{aligned} \tag{15}$$

In order to be commensurate with the optical lattice, here we take $k_2^{\mathrm{L}} = 2\sqrt{3}\pi/3a$. The contours of the magnetic field are plotted in Fig. 10(d). One can find that the total accumulated phases along the nearest-neighbor directions are found to cancel out because of the symmetry of honeycomb lattice. However, the total accumulated phases for the next-nearest-neighbor hopping along the arrowed directions of the dashed lines in Fig. 10(a) are just φ. As a consequence, the total Hamiltonian of this cold atomic system can be described by Eq. (14).

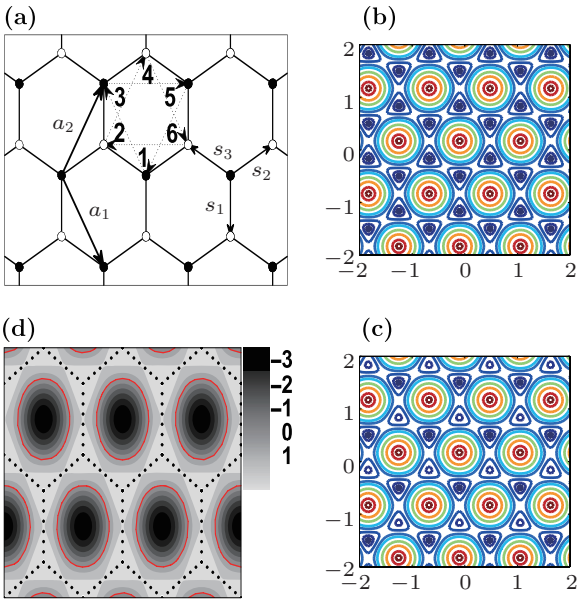


Fig. 10. (a) The Honeycomb lattice structure of graphene, where open and solid circles represent sites in sublattices A and B. $\boldsymbol{a}_1 = (a/2, -\sqrt{3}a/2)$ and $\boldsymbol{a}_2 = (a/2, \sqrt{3}a/2)$ are the unit vectors of the underlying triangular sublattice. s_1, s_2, and s_3 are three vectors pointing from an a site to its three nearest-neighbor sites. (b) and (c) The contours of the lattice potential for $\chi = 2\pi/3$ and $\chi = 39\pi/60$, respectively. The vertical (horizontal) axis represents yk_0^{L}/π (xk_0^{L}/π). (d) Contours of the laser-induced staggered magnetic field.[78]

4.2. Phase diagram

With Fourier transformation into momentum space, the Hamiltonian of system can be written in the spinor basis $(a_{\boldsymbol{k}}, b_{\boldsymbol{k}})^t$ as

$$H_k = h_0(\boldsymbol{k}) + h_x(\boldsymbol{k})\sigma_x + h_y(\boldsymbol{k})\sigma_y + h_z(\boldsymbol{k})\sigma_z, \tag{16}$$

where $h_0(\boldsymbol{k}) = 2t'\cos\varphi\sum_i\cos(\boldsymbol{k}\cdot\boldsymbol{a}_i)$, $h_x(\boldsymbol{k}) = t\sum_i\cos(\boldsymbol{k}\cdot\boldsymbol{s}_i)$, $h_y(\boldsymbol{k}) = t\sum_i\sin(\boldsymbol{k}\cdot\boldsymbol{s}_i)$, and $h_z(\boldsymbol{k}) = M + 2t'\sin\varphi\sum_i\sin(\boldsymbol{k}\cdot\boldsymbol{a}_i)$. The vector $\boldsymbol{h}(\boldsymbol{k}) = [h_x(\boldsymbol{k}), h_y(\boldsymbol{k}), h_z(\boldsymbol{k})]$ is an effective magnetic field of the spinor. The energy spectra has the from

of $E_{\boldsymbol{k}} = h_0(k) \pm |\boldsymbol{h}(\boldsymbol{k})|$, and the energy gap is $|h_z|$, where $h_z = h_z(K_\pm)$ with $K_\pm = \pm\frac{4\pi}{3a}(1,0)$. If $h_z = 0$, the conduction band touches the valence band at the two Dirac points $K_\pm$. The topological properties of the model can be obtained from the field $\boldsymbol{h}(\boldsymbol{k})$. In particular, the lowest energy band has a total Chern number of

$$C = \frac{1}{4\pi}\int_{\mathrm{BZ}} \boldsymbol{h}\cdot(\partial_{k_x}\boldsymbol{h}\times\partial_{k_y}\boldsymbol{h})d^2\boldsymbol{k}. \tag{17}$$

The phase diagram is depicted in Fig. 11(a), in which the solid line is the critical boundary between the normal insulator with $C = 0$ and the Chern insulator with $C = \pm 1$. It is notable that the phase $\varphi = \pi\tan\theta$ can be controllable by simply choosing the laser angle θ, while the energy difference M between sublattice can be tuned by the phase of laser beams. With such controllability, it is promising to realize the exotic topological phase transition between different Chern numbers in Fig. 11(a).

4.3. Detection method

We now turn to establish a direct connection between the topological Cherm number and the atomic density, noting that the latter can be detected with density profile measurements typically used in atomic systems. We first develop a Green function method to calculate the atomic density. The system is actually described by a Dirac-like Hamiltonian which can be obtained by expanding Eq. (16) around two Dirac points. By the substitution of $\boldsymbol{k} = K_\pm + \boldsymbol{p}$, we have $H_\pm = \mp\upsilon_{\mathrm{F}}p_x\sigma_x - \upsilon_{\mathrm{F}}p_y\sigma_y + m_\pm\sigma_z$, where $\upsilon_{\mathrm{F}} = \sqrt{3}at/2$ is the Fermi velocity and $m_\pm = M \pm 3\sqrt{3}t'\sin\varphi$. Under an unitary transformation $\sigma_y H_\pm \sigma_y$, the Dirac Hamiltonian becomes

$$H_\pm = -\upsilon_{\mathrm{F}}p_x\sigma_x - \upsilon_{\mathrm{F}}p_y\sigma_y + m\sigma_z, \tag{18}$$

where $m = \pm m_\pm$ is introduced for simplicity.

It is observed that, once an additional uniform magnetic field B is applied, the conductivity of the system is related to the atomic density according to the Streda formula $\sigma_{xy} = \partial\rho/\partial\mathscr{B}|_{\mu,T}$. Such a magnetic field can be simulated by rotating the optical lattice at a constant frequency $\omega = e\mathscr{B}/2m$. We choose the vector potential as $\mathscr{A}_0 = \mathscr{A}_1 = 0$ and $\mathscr{A}_2 = \mathscr{B}x$. The density in terms of the Green's function for the Dirac Hamiltonian is given by

$$(\mathscr{D} + m)G = 1, \rho = -\mathrm{Tr}[\gamma^0 G(x,x')]|_{x\to x'}, \tag{19}$$

where $\mathscr{D} = \gamma^\tau D_\tau$, with $D_0 = \hbar\partial_0 - \mu$, $D_1 = \hbar\upsilon_{\mathrm{F}}\partial_1$, $D_2 = \hbar\upsilon_{\mathrm{F}}\partial_2 + \mathrm{i}e\upsilon_{\mathrm{F}}\mathscr{B}x$, $\gamma^0 = \sigma_z$, $\gamma^1 = \sigma_y$, and $\gamma^2 = -\sigma_x$ in Euclidean space. From the standard Green function approach, the atomic density is explicitly obtained as

$$\rho_\pm = \left|\frac{\mathscr{B}}{\phi_0}\right|\mathrm{sgn}(\mu)\left[\mathrm{int}\left[\frac{\mu^2 - m_\pm^2}{2\hbar\upsilon_{\mathrm{F}}|e\mathscr{B}|}\right] + \frac{1}{2}\right]\Theta(|\mu| - |m_\pm|)$$
$$\pm\frac{\mathscr{B}}{2\phi_0}\frac{m_\pm}{|m_{\mathrm{p}}m|}\Theta(|m_\pm| - |\mu|), \tag{20}$$

where ϕ_0 is the flux quantum, and int$[x]$ means the largest integer less than x. The second term of Eq. (7) is the atomic density induced into vacuum as $\mu \to 0$ by the uniform magnetic field.

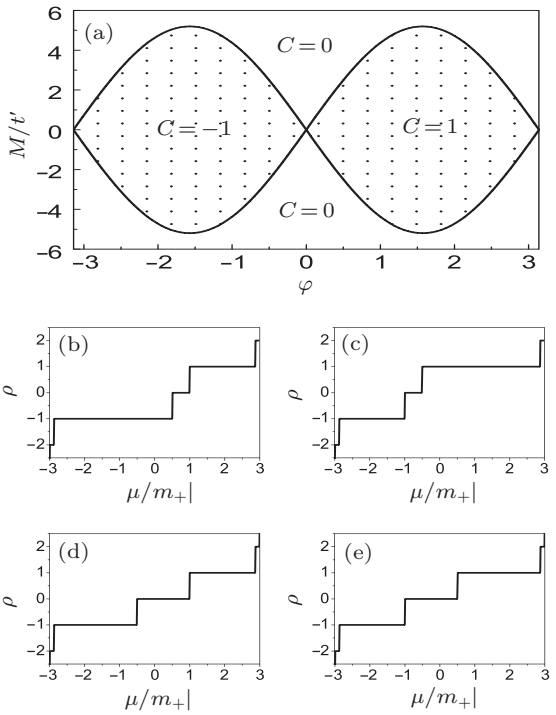


Fig. 11. (a) Phase diagram of the system, where the phase boundary (solid line) corresponds to $h_z = 0$. (b)–(e) Charge density in units of $\mathscr{B}/\phi_0$ for $|m_-| = 0.5|m_+|$ and $e\mathscr{B}\hbar\upsilon_{\mathrm{F}}^2 = 4|m_+|$ as a function of normalized chemical potential μ/m_+ for four different cases: (b) $m_+ < 0 < m_-$, (c) $m_+ > 0 > m_-$, (d) $m_+ < m_- < 0$, and (e) $m_+ > m_- > 0$.[78]

At $\mu = 0$, the Hall conductivity at $\mathscr{B} = 0$ can be obtained from the density by using the Streda formula as $\sigma_{xy} = Ce^2/\hbar$, where the Chern number $C = [\mathrm{sgn}(m_+) - \mathrm{sgn}(m_-)]/2$. In Figs. 11(b)–11(e), the total atomic density $\rho = \rho_+ + \rho_-$ in units of $|\mathscr{B}/\phi_0|$ is plotted for four different cases as a function of the normalized chemical potential $\mu/|m_+|$. We here focus on $\mu = 0$, which is of our main interest. For $m_+ < 0 < m_-$ corresponding to $C = -1$, the atomic density $\rho = -\mathscr{B}/\phi_0 < 0$, as shown in Fig. 11(b). For $m_+ > 0 > m_-$ corresponding to $C = 1$, the density $\rho = \mathscr{B}/\phi_0 > 0$, as shown in Fig. 11(c). For the other two cases, m_+ and m_- have the same sign, corresponding to $C = 0$ and the density $\rho = 0$, as seen from Figs. 11(d) and 11(e). Therefore, a simple direct relation between the Chern number and the atomic density is established as

$$C = \rho\phi_0/\mathscr{B}. \tag{21}$$

The above relation actually provides us a feasible way to experimentally detect the Chern number C in different phases.

In the absence of $\mathscr{B}$, the density of the cold atoms at $\mu = 0$ is first measured, which is denoted as ρ_0. Then, the optical lattice is rotated to generate the effective uniform magnetic field $\mathscr{B}$, and the new density of the cold atoms ρ_1 is measured. If $\rho_1 > \rho_0 (\rho_1 < \rho_0)$, the system is in a Chern insulator phase with Chern number $C = +1(-1)$. If $\rho_1 = \rho_0$, the system behaves like a normal insulator with $C = 0$. Since the density difference is actually quantized in units of $\mathscr{B}/\phi_0$, the above method could be rather robust.

5. Summary

In summary, we have mainly reviewed our recent work on quantum simulation of graphene-like physics with ultracold atoms in optical lattices. We show that ultracold atoms trapped in a honeycomb optical lattice is a direct analogue of graphene, and the Dirac fermions there can be simulated directly in such an optical lattice. With the help of artificial gauge fields, the unconventional Hall effect in graphene-like systems can be simulated in a square optical lattice. Finally, we design a method to generate a staggered magnetic field in a honeycomb lattice for breaking time-reversal symmetry and realize the quantum Hall effect without Landau levels. We also review the related experimental advances on our simulation models.

References

[1] Novoselov K S, Geim A K, Morozov S V, Jiang D, Zhang Y, Dubonos S V, Grigorieva I V and Firsov A A 2004 *Science* **306** 666

[2] Geim A K and Novoselov K S 2007 *Nat. Mater.* **6** 183

[3] Geim A K 2009 *Science* **324** 1530

[4] Castro Neto A H, Guinea F, Peres N M R, Novoselov K S and Geim A K 2009 *Rev. Mod. Phys.* **81** 109

[5] Goerbig M O 2011 *Rev. Mod. Phys.* **83** 1193

[6] Katsnelson M I, Novoselov K S and Geim A K 2006 *Nat. Phys.* **2** 620

[7] Zheng Y and Ando T 2002 *Phys. Rev. B* **65** 245420

[8] Gusynin V P and Sharapov S G 2005 *Phys. Rev. Lett.* **95** 146801

[9] Zhang Y, Tan Y W, Stormer H L and Kim P 2005 *Nature* **438** 201

[10] Novoselov K S, Geim A K, Morozov S V, Jiang D, Katsnelson M I, Grigorieva I V, Dubonos S V and Firsov A A 2005 *Nature* **438** 197

[11] Haldane F D M 1988 *Phys. Rev. Lett.* **61** 20015

[12] Hasan M Z and Kane C L 2010 *Rev. Mod. Phys.* **82** 3045

[13] Lewenstein M, Sanpera A, Ahufinger V, Damski B, Sen A and Sen U 2007 *Adv. Phys.* **56** 243

[14] Bloch I, Dalibard J and Zwerger W 2008 *Rev. Mod. Phys.* **80** 885

[15] Dalibard J, Gerbier F, Juzeliunas G and Ohberg P 2011 *Rev. Mod. Phys.* **83** 1523

[16] Zhang D W, Wang Z D and Zhu S L 2012 *Front. Phys.* **7** 31

[17] Tarruell L, Greif D, Uehlinger T, Jotzu G and Esslinger T 2012 *Nature* **483** 302

[18] Zhu S L, Wang B G and Duan L M 2007 *Phys. Rev. Lett.* **98** 260402

[19] Lin Y J, Compton R L, Garcia K J, Porto J V and Spielman I B 2009 *Nature* **462** 628

[20] Lin Y J, Jimenez-Garcia K and Spielman I B 2011 *Nature* **471** 83

[21] Aidelsburger M, Atala M, Nascimb'ene M, Troztky S, Chen Y A and Bloch I 2011 *Phys. Rev. Lett.* **107** 255301

[22] Zhang J Y, Ji S C, Chen Z, Zhang L, Du Z D, Yan B, Pan G S, Zhao B, Deng Y J, Zhai H, Chen S and Pan J W 2012 *Phys. Rev. Lett.* **109** 115301

[23] Wang P, Yu Z Q, Fu Z, Miao J, Huang L, Chai S, Zhai H and Zhang J 2012 *Phys. Rev. Lett.* **109** 095301

[24] Cheuk L W, Sommer A T, Hadzibabic Z, Yefsah T, Bakr W S and Zwierlein M W 2012 *Phys. Rev. Lett.* **109** 095302

[25] LeBlanc L J, Williams R A, Beeler M C, Perry A R and Spielman I B 2012 *Phys. Rev. Lett.* **108** 225303

[26] Struck J, Ölschlaĝer C, Weinberg M, Hauke P, Simonet J, Eckardt A, Lewenstein M, Sengstock K and Windpassinger P 2012 *Phys. Rev. Lett.* **108** 225304

[27] Struck J, Weinberg M, Ölschläger C, Windpassinger P, Simonet J, Sengstock K, Höpner R, Hauke P, Eckardt A, Lewenstein M and Mathey L 2013 *Nat. Phys.*

[28] Aidelsburger M, Atala M, Lohse M, Barreiro J T, Paredes B and Bloch I arXiv:1308.0321

[29] Miyake H, Sivloglou G A, Kennedy C J, Burton W C and Ketterle W arXiv:1308.1431

[30] LeBlanc L J, Beeler M C, Jimenez-Garcia K, Perry A R, Sugawa S, Williams R A and Spielman I B 2013 *New J. Phys.* **15** 073011

[31] Qu C, Hamner C, Gong M, Zhang C and Engels P 2013 *Phys. Rev. A* **88** 021604

[32] Zhu S L, Fu H, Wu C J, Zhang S C and Duan L M 2006 *Phys. Rev. Lett.* **97** 240401

[33] Liu X J, Liu X, Kwek L C and Oh C H 2007 *Phys. Rev. Lett.* **98** 026602

[34] Beeler M C, Williams R A, Jimenez-Garcia K, LeBlanc L J, Perry A R and Spielman I B 2013 *Nature* **498** 201

[35] deGail R, Fuchs J N, Goerbig M O, Piechon F and Montambaux G 2012 *Physica B* **407** 1948

[36] Lee K L, Gremaud B, Han R, Englert B G and Miniatura C 2009 *Phys. Rev. A* **80** 043411

[37] Block J K and Nygaard N 2009 *Phys. Rev. A* **80** 043411

[38] Zhao E and Paramekanti A 2006 *Phys. Rev. Lett.* **97** 230404

[39] Chen Z and Wu B 2011 *Phys. Rev. Lett.* **107** 065301

[40] Sun F, Yu X L, Ye J, Fan H and Liu W M 2013 *Sci Rep.* **3** 2119

[41] Poletti D, Miniatura C and Gremaud B 2011 *Europhys. Lett.* **93** 37008

[42] Bermudez A, Goldman N, Kubasiak A, Lewenstein M and Martin-Delgado M A 2010 *New J. Phys.* **12** 033041

[43] Wu C and Sarma S D 2008 *Phys. Rev. B* **77** 235107

[44] Gomes K K, Mar W, Ko W, Guinea F and Manoharan H C 2012 *Nature* **483** 306

[45] Bellec M, Kuhl U, Montambaux G and Mortessagne F 2013 *Phys. Rev. Lett.* **110** 033902

[46] Koghee S, Lim L K, Goerbig M O and Smith C M 2012 *Phys. Rev. A* **85** 023637

[47] Lifshitz I M 1960 *Sov. Phys. JETP* **11** 1130

[48] Bercioux D, Urban D F, Grabert H and Häsler W 2009 *Phys. Rev. A* **80** 063603

[49] Bercioux D, Goldman N and Urban D F 2011 *Phys. Rev. A* **83** 023609

[50] Shen R, Shao L B, Wang B and Xing D Y 2010 *Phys. Rev. B* **81** 041410

[51] Satija I I, Dakin D C, Vaishnav J Y and Clark C W 2008 *Phys. Rev. A* **77** 043410

[52] Hou J M, Yang W X and Liu X J 2009 *Phys. Rev. A* **79** 043621

[53] Lim L K, Smith C M and Hemmerich A 2008 *Phys. Rev. Lett.* **100** 130402

[54] Lim L K, Lazarides A, Hemmerich A and Smith C M 2009 *Europhys. Lett.* **88** 36001

[55] Lim L K, Hemmerich A and Smith C M 2010 *Phys. Rev. A* **81** 023404

[56] Goldman N, Kubasiak A, Bermudez A, Gaspard P, Lewenstein M and Martin-Delgado M A 2009 *Phys. Rev. Lett.* **103** 035301

[57] Liu X J, Liu X, Wu C and Sinova J 2010 *Phys. Rev. A* **81** 033622

[58] Kennett M P, Komeilizadeh N, Kaveh K and Smith P M 2011 *Phys. Rev. A* **83** 053636

[59] Yang M and Zhu S L 2010 *Phys. Rev. A* **82** 064102

[60] Bermudez A, Mazza L, Rizzi M, Goldman N, Lewenstein M and Martin-Delgado M A 2010 *Phys. Rev. Lett.* **105** 190404

[61] Lepori L, Mussardo G and Trombettoni A 2010 *Europhys. Lett.* **92** 50003
[62] Vaishnav J Y and Clark C W 2008 *Phys. Rev. Lett.* **100** 153002
[63] Juzeliūnas G, Ruseckas J, Lindberg M, Santos L and Öhberg P 2008 *Phys. Rev. A* **77** 011802
[64] Merkl M, Zimmer F E and Öhberg P 2008 *Europhys. Lett.* **83** 54002
[65] Zhu S L, Zhang D W and Wang Z D 2009 *Phys. Rev. Lett.* **102** 210403
[66] Song J J and Foreman B A 2009 *Phys. Rev. A* **80** 045602
[67] Zhang Q, Gong J and Oh C H 2010 *Phys. Rev. A* **81** 023608
[68] Zhu S L, Shao L B, Wang Z D and Duan L M 2011 *Phys. Rev. Lett.* **106** 100404
[69] Zhang D W, Xue Z Y, Yan H, Wang Z D and Zhu S L 2012 *Phys. Rev. A* **85** 013628
[70] Zhang D W, Shao L B, Xue Z Y, Yan H, Wang Z D and Zhu S L 2012 *Phys. Rev. A* **86** 063616
[71] Zwierlein M W, Schirotzek A, Schunck C H and Ketterle W 2006 *Nature* **311** 492
[72] Partridge G B, Li W, Kamar R I, Liao Y and Hulet R G 2006 *Nature* **311** 503
[73] Stamper-Kurn D M, Chikkatur A P, Gorlitz A, Inouye S, Gupta S, Pritchard D E and Ketterle W 1999 *Phys. Rev. Lett.* **83** 2876
[74] Kohl M, Moritz H, Stoferle T, Günter K and Esslinger T 2005 *Phys. Rev. Lett.* **94** 080403
[75] Mei F, Zhu S L, Feng X L, Zhang Z M and Oh C H 2011 *Phys. Rev. A* **84** 023662
[76] Jaksch D and Zoller P 2003 *New J. Phys.* **5** 56
[77] Watanabe H, Hatsugai Y and Aoki H 2010 *Phys. Rev. B* **82** 241403
[78] Shao L B, Zhu S L, Sheng L, Xing D Y and Wang Z D 2008 *Phys. Rev. Lett.* **101** 246801
[79] Umucalilar R O, Zhai H and Oktel M O 2008 *Phys. Rev. Lett.* **100** 070402
[80] Mei F, Zhu S L, Zhang Z M, Oh C H and Goldman N 2012 *Phys. Rev. A* **85** 013638
[81] Wu C J 2008 *Phys. Rev. Lett.* **101** 186807
[82] Zhang M, Hsiang-hsuan H, Zhang C and Wu C 2011 *Phys. Rev. A* **83** 023615
[83] Alba E, Fernandez-Gonzalvo X, Mur-Petit J, Pachos J K and Garcia-Ripoll J J 2011 *Phys. Rev. Lett.* **107** 235301
[84] Goldman N, Anisimovas E, Gerbier F, Ohberg P, Spielman I B and Juzeliunas G 2013 *New J. Phys.* **15** 013205